Conducting thermal energy to the membrane/water interface for the enhanced desalination of hypersaline brines using membrane distillation

Jingbo Wang[a†], Yiming Liu[a†], Unnati Rao[a], Mark Dudley[b], Navid Dehdari Ebrahimi[c], Jincheng Lou [b], Fei Han[d], Eric M.V. Hoek[a], Nils Tilton[b], Tzahi Y. Cath[e], Craig S. Turchi[f], Michael B. Heeley[g], Y. Sungtaek Ju[c], David Jassby[a*]

[a] University of California Los Angeles (UCLA), Department of Civil & Environmental Engineering, California NanoSystems Institute and Institute of the Environment & Sustainability, Los Angeles, CA, USA
[b] Colorado School of Mines, Department of Mechanical Engineering, Golden, CO, USA
[c] UCLA, Department of Mechanical and Aerospace Engineering, Los Angeles, CA, USA
[d] Hebei University of Technology, School of Civil and Transportation Engineering, Tianjin, China
[e] Colorado School of Mines, Department of Civil and Environmental Engineering, Golden, CO, USA
[f] Buildings & Thermal Science Center, National Renewable Energy Laboratory, Golden, CO, USA
[g] Colorado School of Mines, Division of Economics and Business, Golden, CO, USA

*Corresponding author [tel: (310) 825-1346; email: jassby@ucla.edu]
[†]These authors contributed equally

Abstract

Membrane distillation (MD) is a membrane-based thermal desalination process capable of treating hypersaline brines. Standard MD systems rely on preheating the feed to drive the desalination process. However, relying on the feed to carry thermal energy is limited by a decline of the thermal driving force as the water moves across the membrane, and temperature polarization. In contrast, supplying heat directly into the feed channel, either through the membrane or other channel surfaces, has the potential of minimizing temperature polarization, increasing single-pass water recoveries, and decreasing the number of heat exchangers in the system. When solar thermal energy can be utilized, particularly if the solar heat is optimally delivered to enhance water evaporation and process performance, MD processes can potentially be improved in terms of energy efficiency, environmental sustainability, or operating costs. Here we describe an MD process using layered composite membranes that include a high-thermal-conductivity layer for supplying heat directly to the membrane-water interface and the flow channel. The MD system showed stable performance with water flux up to 9 L/m^2/hr, and salt rejection >99.9% over hours of desalinating hypersaline feed (100 g/L NaCl). In addition to bench-scale system, we developed a computational fluid dynamics model that successfully described the transport phenomena in the system.

Keywords: membrane distillation, thermal desalination, hypersaline water treatment, gained output ratio, specific energy consumption

1. Introduction

Membrane distillation (MD) is a membrane-based thermal desalination process that involves the evaporation of water through a microporous, hydrophobic membrane. Common MD membrane materials include polyvinylidene fluoride (PVDF), polytetrafluoroethylene (PTFE), and polypropylene (PP) [1]. In comparison to other membrane and thermal desalination processes, MD has several advantages when treating high salinity waters, including lower operating temperature and thermal energy demand than some conventional thermal distillation processes, lower operating pressure and electrical energy demand than conventional reverse osmosis processes, and the capability to treat water of nearly any salinity up to saturation [1–4]. Though pressure-driven desalination processes such as RO are less energy intensive than MD, they are limited to salinity below 70 g/L [5]. In contrast, the performance of MD is comparably less sensitive to feedwater salinity, making it attractive for desalinating high-salinity waste streams [3,6,7].

In a standard MD system, saline feed water is heated before contacting the membrane that separates the hot feed from the distillate. As warm feed flows over the membrane, water evaporates at the water/membrane interface, diffuses through the membrane pores, and condenses in the colder permeate side [8,9]. In this design, the hot feed stream serves as the thermal energy carrier to drive the desalination process; however, the reliance on the feed to carry thermal energy has limitations, including temperature polarization and overall feed stream temperature drop, which cause the driving force for evaporation to rapidly decline along the membrane (Fig. 1). Temperature polarization is caused by heat loss through the membrane, which occurs due to heat advection by the vapor and heat conduction through the vapor-filled pores and solid polymer phase of the membrane. Temperature polarization limits the thermal

efficiency of MD and connects it to feed side hydrodynamics [4]. Due to temperature polarization, the temperature at the membrane surface on the feed side ($T_{m,f}$) may be substantially lower than the bulk feed temperature ($T_{b,f}$) [4,7,10–15].

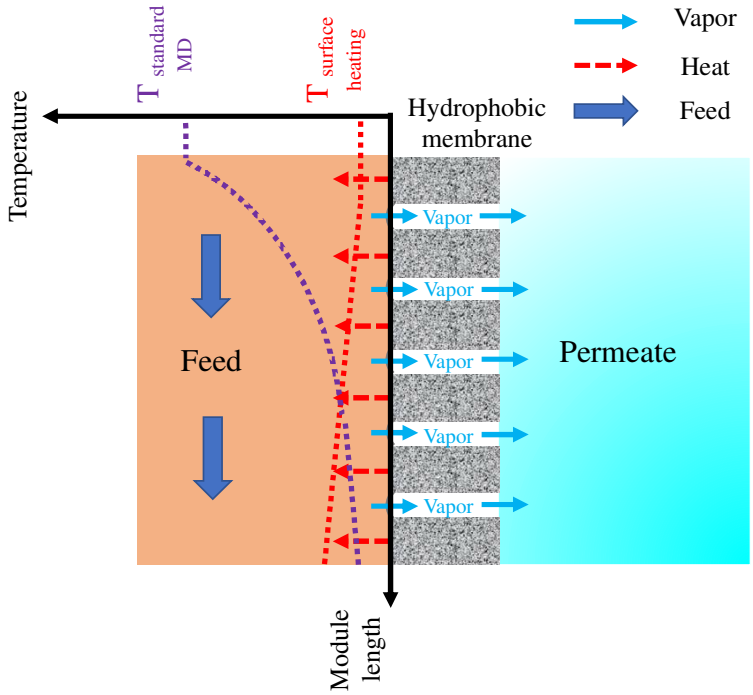

Fig. 1. Temperature profile of a standard MD and a direct heating MD system with localized heating at the feed/membrane interface.

Integrating renewable energy as the heat source is important for MD to become more practical and economically viable [16–19]. Several studies have successfully operated conventional MD systems by preheating the feed using solar energy. However, this approach still suffers from temperature polarization and feed temperature drop within the MD system [20–26]. In contrast, providing thermal energy directly to the membrane-water interface (where evaporation occurs) and/or through another surface in the feed channel has the potential of minimizing temperature polarization (Fig. 1), increasing single-pass water recovery, and decreasing the number of heat exchangers in the system, thus improving the energy efficiency of

89 the lab-scale thermal process [27,28]. Several studies [4,29–36] have demonstrated the feasibility
90 and effectiveness of direct heating, either by solar-driven photothermal membranes [4,29–34] or
91 resistively-heated membranes [35,36]. However, studies implementing photothermal membranes
92 report low water fluxes (below 2 L/m^2/hr (LMH)) under standard or even concentrated solar
93 illumination [4,29–34]. Therefore, producing reasonable desalination rates requires very large
94 membrane surface areas to be exposed to sunlight, complicating system design and increasing
95 capital costs.

96 In this study, we report on an MD process in which the full length of the feed channel is
97 actively heated by supplying heat to thermally conducting layers that were incorporated into the
98 system (Fig. 2). We test the performance of our novel approach by treating hypersaline feeds
99 with a bench-scale vacuum membrane distillation (VMD) system. VMD was chosen for its
100 minimal conductive heat losses, due to the low thermal conductivity of vacuum on the distillate
101 side [37]. The system showed stable performance with water flux up to 9 LMH, and salt rejection
102 >99.9% over hours of operation, with heat only provided through the thermally conducting
103 layers. Optimum system configuration, operating conditions, and specific energy consumptions
104 are discussed. To complement the experimental studies, a computational fluid dynamics model
105 was developed to describe the transport phenomena and explain how operating conditions impact
106 vapor production and temperature polarization. This VMD process can potentially provide a
107 solution to desalinating highly concentrated brines at a lower cost.
108

109 ## 2. Materials and methods

110 ### *2.1.* Materials

111 The polymeric membrane materials used in this study are hydrophobic PP membranes (3M,
112 Charlotte, NC) with a 100 μm thickness, 0.2 μm pore size, and 70% porosity. The thermally
113 conducting layers were aluminum shims (flat aluminum sheets placed in the feed channel, not in
114 direct contact with membrane) with a thickness of 250 μm (McMaster-Carr, Los Angeles, CA),
115 and aluminum meshes (mesh size 120×120) with a thickness of 203 μm, an opening size of 109
116 μm, and an open area of 27%, that were in direct contact with the membrane either in the
117 permeate channel or in the feed channel (Fig. 2). Here, the permeate does not imply any physical
118 permeation of liquid water through the membrane; instead, it refers to the permeation of water
119 vapor. The membrane coupon, aluminum shim piece, and aluminum mesh piece were cut from
120 flat sheets provided by the manufacturers and used directly without further modification. The
121 synthetic hypersaline feed contained 100 g/L NaCl (~3 times seawater salinity) at room
122 temperature. The sodium chloride was ACS grade with 99% or greater purity (Fisher Scientific,
123 Pittsburgh, PA) and was used as received.
124
125 ***2.2.*** **Direct heating VMD experiments**
126 The experiments were performed using a fully instrumented and automated laboratory-scale
127 cross-flow VMD system with an Acetal membrane flow cell (Fig. 2a). The membrane cell
128 housed a flat sheet membrane with an effective area of 40 cm^2 (4 cm × 10 cm). The height of the
129 feed and distillate flow channels were 4 mm. No spacers were used in the feed channel. A piece
130 of aluminum (Al) mesh and/or a piece of Al shim were used as the thermal conducting layer,
131 both with a size of 15 cm × 12 cm, with the shim placed in the feed channel (not in contact with
132 the membrane) and the mesh placed in contact with the membrane either in the feed channel or
133 in the permeate channel (Fig. 2). These Al thermal conductors were connected to a heat source

and used to deliver heat into the flow channel (more on this below). A peristaltic pump (Cole Parmer, Pump Drive Model 7553-70, Pump Head Model 77200-50, Vernon Hills, IL) with temperature resistant tubing circulated the feed solution, with the flow rates (0.4-1.6 L/min) controlled by the pump controller. A vacuum pump (JB Industries, Model Number DV-85N, Aurora, IL) generated a vacuum in the range of 0.90-0.99 bar (vacuum gauge reading) on the distillate side of the membrane. The absolute pressure on the distillate side was determined by subtracting the pressure from the vacuum pump gauge from the atmospheric pressure (for example, 0.99 bar vacuum pump gauge reading corresponds to an absolute pressure of 1 - 0.99 = 0.01 bar).

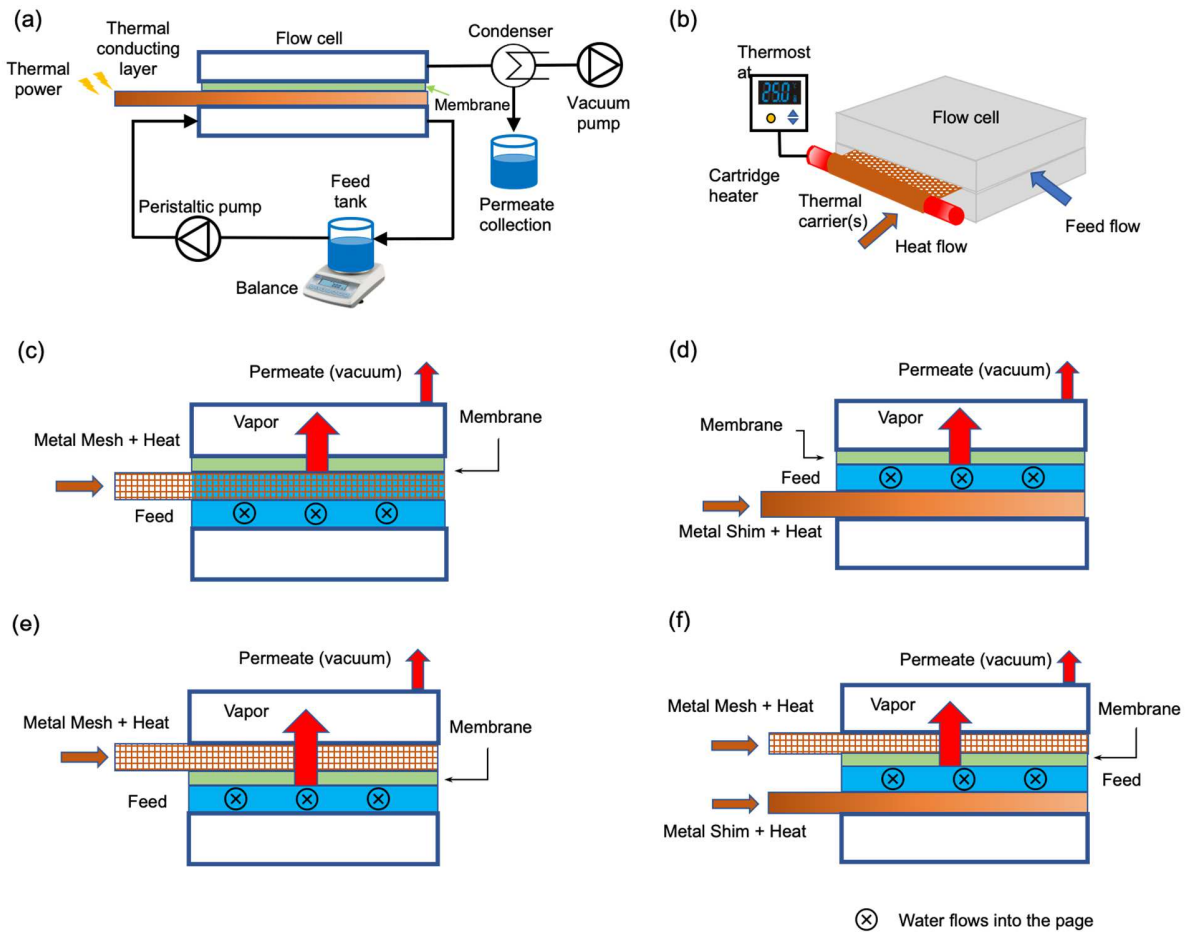

Fig. 2. (a) Schematic of a fully instrumented and automated laboratory-scale direct heating MD system operating in vacuum-assisted mode. The acetal membrane flow cell houses a flat sheet

membrane, and thermal conducting layers that are coupled with thermal power. (b) Schematic of direct heating MD cell and heat source coupling system. Thermal carrier(s) were wrapped around a cartridge heater to mimic the coupling with solar power. The thermostat was used to control heat input to the system. (c) – (f) demonstrate the schematic of the direct heating MD cell configurations: (c) mesh is placed in the feed stream as the only thermal carrier, (d) shim is placed in the feed stream as the only thermal carrier, (e) mesh is on top of membrane in the permeate stream as the only thermal carrier, and (f) both shim and mesh are used as thermal carriers with shim being placed in the feed stream and mesh being placed in permeate stream. Water vapor forms at the water/membrane interface. The heat flow and feed flow directions are perpendicular.

Temperature sensors (Vktech, Model Number DS18b20, Shenzhen, China) monitored the feed temperature at the feed channel entrance and outlet. Salt concentrations in the distillate (C_p, M) and feed (C_F, M) were measured using a conductivity meter (Thermo Fisher Scientific, Orion Star A322, Waltham, MA), and used to calculate observed salt rejection, R, using Eq. 2:

$$R = 1 - \frac{C_p}{C_F} \quad (2)$$

The distillate flux was determined by measuring the mass change of the feed tank in real time using a scale (Ohaus, Model Number PX2202, Parsippany, NJ) set to automatically log mass data every 5 s. The feed tank was insulated with foam to minimize heat losses.

Heat was delivered to the membrane/water interface and/or the flow channel by heat conduction through the metallic thermal carriers (Al shim and mesh). Al shim and mesh were chosen to serve as the thermal conducting layer because of their good thermal conductivity, excellent mechanical strength, and low cost. When the aluminum mesh was installed in the system, the mesh was always placed in close contact with the membrane (either in the feed or the permeate) to provide surface heating. When placing the mesh on the permeate side, the mesh can be kept corrosion free and the heat is not anticipated to be lost to the environment because of the low thermal conductivity of a vacuum. Instead, the heat is expected to conduct across the membrane to the membrane/water interface. The shim was placed close to, but not in direct contact with, the

173 membrane (it was placed on the feed wall opposite the membrane – the stiffness of the shim
174 allowed it to keep its position away from the membrane surface without the need for a spacer).
175 Several configurations with different thermal conducting layers were tested (Fig. 2c-2f).
176 Simulated concentrated solar heat was provided by a cartridge heater with an internal
177 temperature sensor (McMaster-Carr, Los Angeles, CA); heat output from the heater was
178 controlled by a thermal stat (Inkbird, Shenzhen, China). To couple the heater to the thermal
179 carriers (mesh and shim), the thermal carriers were wrapped around the heater, with fiberglass
180 insulation packaged around the entire assembly to minimize heat losses (Fig. 2b).
181 Experiments were performed to evaluate the variation of system behavior when treating high
182 salinity feed (100 g/L NaCl) within the following range of operating conditions:
183 - System configuration (mesh only on the feed side, shim only on the feed side, mesh only
184 on the permeate side, shim on the feed side and mesh on the permeate side)
185 - Heat source temperature (20 °C, 140 °C, 240 °C, 350 °C, 420 °C)
186 - Permeate absolute pressure (0.01 bar, 0.04 bar, 0.1 bar)
187 - Feed crossflow velocity (4 cm/s, 10 cm/s, 16 cm/s)

188 For each set of experiments, the permeate flux was calculated using the slope of the linear
189 regression of the feed mass change over time, divided by the effective membrane area. Under
190 each set of conditions, flux data were collected for at least 2 h after the system stabilized.
191

192 ### *2.3.* Characterization of Al shim and mesh

193 The thermally conducting metallic layers were characterized to evaluate potential corrosion
194 after long-term use in high salinity solutions at elevated temperature. Their surface morphologies
195 were analyzed using scanning electron microscopy (SEM) (Zeiss Supra 40 VP, Carl Zeiss

196 Microscopy LLC, NY). For that purpose, samples were secured on SEM stubs using double-
197 sided carbon tape before imaging. Quantitative analysis and surface elemental mapping were
198 also carried out using energy-dispersive X-ray spectroscopy (EDAX), which is a module
199 included with the Zeiss Supra SEM.
200
201 ***2.4.*** **Energy performance**
202 In a typical VMD system, the energy requirements include [26]: (i) the thermal energy
203 needed to vaporize feed water; (ii) the electrical energy required to create vacuum; and (iii) the
204 electrical energy needed to circulate the feed. In a well-insulated VMD system, thermal energy is
205 the largest energy component, increasing sharply with increasing feed temperature [26]. The
206 evaluation of the energy consumption of an MD system is based on the quantities of energy
207 consumed and the quantity of treated water. We chose specific energy consumption (SEC), a
208 commonly used parameter, to evaluate process performance [38]. Another performance indicator,
209 gained output ratio (GOR), of this system is defined, and investigated based on the impact of
210 operating conditions (see Section S4 in SI).
211 To quantify the heat flux delivered to the membrane module by the thermal carriers, the
212 thermal conductivity of the thermally conducting layer, k_{eff} (W/m·K), was measured (see Section
213 S1 in SI), with $\dot{Q}_{heat}$ estimated by
214 $$\dot{Q}_{heat} = -k_{eff} A \frac{\Delta T}{\Delta x} \quad (3)$$
215 where A (m^2) is the cross-sectional area of the thermally conducting layer, ΔT (K) and Δx (m)
216 are the temperature difference and the distance between two specified points on the thermally
217 conducting layer along the direction of heat transfer, respectively. In this study, type K
218 thermocouples (AWG 24 with Kapton insulation, Minnesota Measurement Instruments LLC,

Minnetrista, MN) were taped to the Al shim and Al mesh surface to monitor temperature and obtain temperature gradient $\frac{\Delta T}{\Delta x}$ (K/m).

SEC (kJ/kg) is defined as the amount of total energy supplied (heat and electrical energy in this case) to produce a unit mass of pure water, which can be calculated as: [39]

$$\mathrm{SEC} = \mathrm{STEC} + \mathrm{SEEC} \tag{4}$$

where STEC (kJ/kg) is the specific thermal energy consumption, or the specific heat consumption, which can be calculated as [40],

$$\mathrm{STEC} = \frac{\dot{Q}_{heat}}{\dot{m}_{per}} \tag{5}$$

and SEEC (kJ/kg) is the specific electrical energy consumption defined as the amount of electrical energy consumed ($\dot{E}$, kJ/s) to produce a unit mass of pure water [41]:

$$\mathrm{SEEC} = \frac{\dot{E}}{\dot{m}_{per}} \tag{6}$$

The electrical energy consumption is composed of the energy needed to induce vacuum on the permeate side and to circulate the feed. Thus, the rate of electrical energy input Ė (kJ/s) is calculated as [42],

$$\dot{E} = \dot{E}_{vac} + \dot{E}_{cir} \tag{7}$$

$$\dot{E}_{vac} = \frac{3.35\times10^{-3}}{\eta_{vac}} T_p q_0 \ln(\frac{P_{atm}}{P_{vac}}) \tag{8}$$

$$\dot{E}_{cir} = \frac{\dot{V}_f \Delta P}{\eta_{cir}} \tag{9}$$

where, $\dot{E}_{cir}$ (kJ/s) and $\dot{E}_{vac}$ (kJ/s) are the rate of electrical energy consumption of the feed flow pump and the vacuum pump, respectively; η_{cir} and η_{vac} are the efficiency of feed and vacuum pump, respectively; $\dot{V}_f$ (m^3/s) is the volumetric flow rate of the feed solution; ΔP (Pa) is the feed bulk pressure difference between the inlet and outlet; T_p is the permeate temperature (K), and q_0

240 (L/min) is the flow rate of the gas (e.g., water vapor, leaking air) to be evacuated from the
241 permeate line. P_{atm} (Pa) and P_{vac} (Pa) are the atmospheric and vacuum pressures, respectively
242 [42].
243
244
245
246 **3. Results and discussion**
247 ***3.1.*** **Thermal carrier and heat input**
248 Unlike conventional VMD processes, where the feed stream is heated before entering the
249 cell, feed solution was pumped directly to our heated VMD system at ambient temperature.
250 Therefore, the only thermal energy input (i.e., driving force) to the system was the heat
251 conducted by the thermal carriers. As the heat transfer efficiency between heat source and
252 thermal conducting layer could vary depending on the form of the heat source and coupling
253 techniques, both of which were beyond the scope of this study, we chose to calculate the heat
254 flux that was directly delivered into the system (Fig. S1), which provides a more precise analysis
255 of system performance given a certain heat input, regardless of heat source. Based on Eq. 3, a
256 higher thermal conductivity of the thermal carrier, a larger cross-sectional area, or a higher
257 temperature gradient would all contribute to a larger thermal energy input to the system, which
258 would potentially provide a higher driving force and yield higher permeate flux. The two thermal
259 carriers tested in this study were evaluated for their heat conducting performance. In terms of the
260 dimensions, both Al shim and mesh had the same width, with the Al shim being 51 μm thicker
261 than the Al mesh. The thermal conductivity of the Al shim and Al mesh were determined to be
262 203.4 $\pm$ 2.2 W/m·K and 20.0 $\pm$ 5.0 W/m·K, respectively. The difference in the geometries of Al

shim and mesh explains the difference in their thermal conductivity – as a thin and porous material, the effective thermal conductivity of the Al mesh is only a fraction of a piece of solid Al shim. The temperature gradient on the thermal carrier is related to both the thermal conductor and the heat source temperature (for details on the specific temperatures measured on the shim and mesh, see temperature profiles in the SI (Fig. S2)). For example, when the heat source temperature was set to 140 °C, the temperature gradient on the Al shim and mesh were determined to be 25.6 ± 3.6 K/cm and 57.9 ± 13.0 K/cm, respectively.

Although the temperature gradient on the Al mesh is twice that on the Al shim, the thermal conductivity of the Al mesh is only ~10% that of the Al shim. Therefore, the overall thermal energy delivered by the Al mesh is smaller than that delivered by the Al shim. In the case of a heat source temperature of 140 °C and 240 °C, the temperature gradient on the Al mesh was 57.9 ± 13.0 K/cm and 98.1 ± 22.3 K/cm, respectively. For the configurations including shim as the thermal carrier, 140 °C was determined to be the highest possible temperature at the heat source, as higher temperatures melted the acetal flow cell. However, the lower thermal conductivity of the mesh allowed far higher temperatures to be applied to it, with temperatures as high as 420 °C being tolerated. The temperature range studied here is higher than typical MD systems because this VMD system is intended to couple with a solar collection system and conduct solar thermal heat to drive the MD process. These temperatures are well within the temperature levels that can be achieved by solar thermal collectors [43,44].

Based on the measured temperature profiles (Fig. S2), the thermal input applied in all the scenarios were calculated (Fig. 3 and Fig. S7). The results indicated that the Al shim, which has the higher thermal conductivity, delivered more heat into the system than the Al mesh, given the

same heat source temperature. In addition, higher heat source temperatures helped to deliver more heat with the same thermal carrier.

3.2. Water flux

The driving force for the desalination process is a partial vapor pressure difference across the membrane, which is affected by both heat and vacuum. The effect of heat and vacuum on the overall system performance were tested, and the results are shown in Fig. 3a. In these experiments, the permeate pressure was fixed at 0.01 bar and the crossflow velocity was kept at 4 cm/s. When heat was applied to the system by connecting the thermal carrier(s) to a cartridge heater operating at 140 °C, the system showed the highest flux (5.33 ± 0.32 LMH) with the shim+mesh configuration, followed by the shim-only configuration (4.6 ± 0.94 LMH), and then mesh-only on the permeate stream configuration (2.6 ± 0.35 LMH). When the heater was turned off (represented by the 20 °C bars in Fig. 3a), the flux declined to approximately 2 LMH, regardless of the thermal carrier configuration. The differences in water vapor flux between the heated and non-heated sets indicate effective heat delivery into the system through the thermal carriers, under certain conditions.

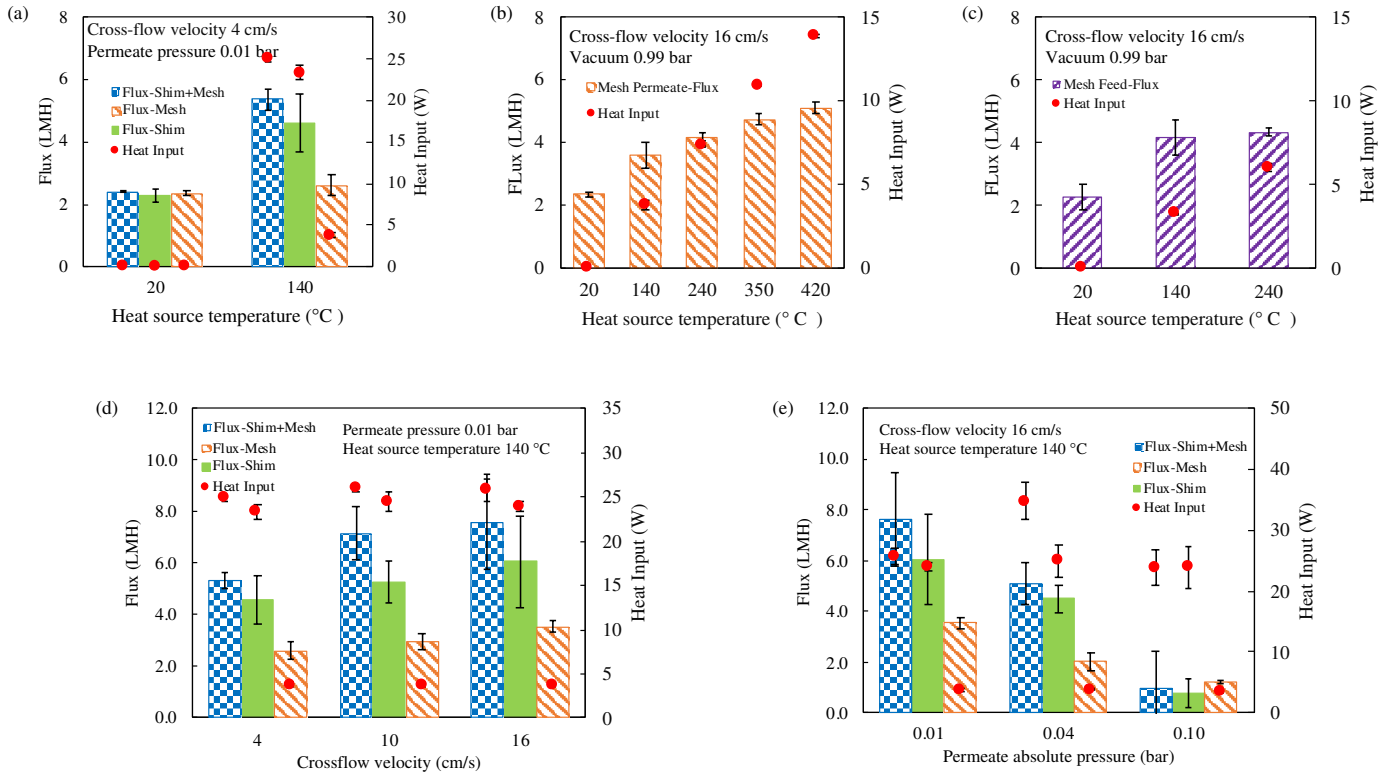

Fig. 3. Heat input and corresponding vapor flux and in 2 h long tests with different system configurations as indicated in the figures: only shim in the feed stream, only mesh in the feed stream, only mesh on the permeate side, or only shim in the feed stream and only mesh on the permeate side as the thermal carrier(s). All tests were performed with feed water contains 100 g/L NaCl. Measured water flux values are shown in bars (values correspond to the y-axis on the left) as a function of (a)-(c) temperature, (d) crossflow velocity, and (e) permeate pressure, at the conditions specified. The heat input values are shown in red dots (values correspond to the y-axis on the right).

The results from the heated set suggest that higher heat input increases the flux, which is expected. When the heat source temperature is constant, the shim+mesh configuration was able to deliver the highest amount of heat among all the configurations (Fig. 3a), likely due to the extra thermal carrier compared to a single thermal carrier configuration. In the scenarios where only one thermal carrier was used, the shim delivered more heat (24.3 ± 0.8 W) than the mesh (3.7 ± 0.3 W) because of its higher thermal conductivity.

316 To further evaluate the change of vapor flux as a function of heat input, additional sets of
317 experiments were conducted for the case when only the mesh was used as the thermal carrier. As
318 shown in Fig. 3b (mesh on the permeate side), as the heat source temperature increased from 20
319 °C to 420 °C (corresponding to an increase of the heat input from 0 to 13.9 ± 0.1 W), the
320 distillate flux increased from 2.3 ± 0.1 LMH to 5.1 ± 0.2 LMH. Similarly, in Fig. 3c (mesh on
321 the feed side), the distillate flux increased from 2.3 ± 0.4 LMH to 4.3 ± 0.1 LMH as the heat
322 source temperature increased from 20 °C to 240 °C (corresponding to an increase of heat input
323 from 0 to 6.0 ± 0.2 W). Between these two surface heating configurations where mesh was the
324 only thermal carrier, the flux showed no significant difference between placing the mesh on the
325 feed or distillate side (Fig. 3b-3c), which indicates that surface heating can be achieved with
326 mesh on the permeate as effectively as placing the mesh in the feed stream. The reason for this is
327 likely that while the PP membrane has poor thermal conductivity (0.11 – 0.2 W/m K) [45], the
328 membrane's small thickness still allows ample heat to reach the membrane/water interface when
329 it is applied to the mesh in the distillate stream. When heat is added to the mesh while it is
330 immersed in the feed stream, it is also possible that the heat rapidly dissipates (i.e., it is carried
331 away by the water), leading to uneven heat distribution across the membrane surface; this
332 phenomenon is captured in our modeling effort, and described below. Considering that placing
333 the mesh in the warm saline feed can lead to corrosion (see SI Section S3), the configuration of
334 mesh in the feed stream was not investigated further and the rest of the discussion will focus on
335 the results from other configurations (Fig. 2d-2f).
336 In the series of experiments conducted to determine the impact of the crossflow velocity on
337 the membrane flux, we observed that the flux increases as crossflow velocity increased for all
338 system configurations (Fig. 3d). Some conventional MD systems showed similar behavior, and

this phenomenon was attributed to the decrease in temperature polarization as crossflow velocity increases [3,7]. Our numerical analysis (Section 3.4) also supported that; in these tested conditions higher feed velocity helped to reduce the impact of temperature polarization, thus increasing vapor flux. This result is highly beneficial because it allows the system to operate at crossflow velocities that can minimize membrane fouling while still taking advantage of surface and feed-stream heating with enhanced flux. It is likely that in a longer membrane module the flow velocity would further strengthen the impact on flux, as any heat not used for flux generation would be carried further down the module, increasing the bulk fluid temperature, and increasing water flux. Therefore, the results in Fig. 3d represent a lower bound on flux, with longer modules likely leading to higher fluxes, given a certain level of heat input (see section 3.4 for more data and discussion).

In the set of experiments used to determine the impact of permeate vaccum pressure on membrane flux, the heat source temperature and cross-flow velocity were fixed while different vacuums were applied (Fig. 3e). Regardless of the configuration, lower permeate pressure (i.e., higher vacuum level) lead to higher flux, with the vapor flux being highly sensitive to vacuum pressure, and flux dropping substantially (from ~8 LMH to ~1 LMH) when the permeate pressure increased from 0.01 bar to 0.10 bar. These trends can be explained by the fact that flux is proportional to the vapor pressure difference between feed side and permeate side, shown as

$$J = A_m(P_{m,f} - P_v) \quad (10)$$

where J is the permeate flux, A_m is the membrane permeability, $P_{f,m}$ is the partial vapor pressure at feed/membrane interface, P_v is the absolute pressure on the permeate side. $P_{m,f}$ is determined by the temperature at the feed/membrane interface $T_{m,f}$ (K), which can be expressed in Antoine Equation [46],

362 $$P_{m,f} = (\frac{1}{1+m}) \exp(23.1964 - \frac{3816.44}{T_{m,f}-46.13}) \quad (11)$$

363 where m is the molar fraction of salt at the feed/membrane interface. The increase of permeate
364 pressure (P_v) directly impacts the flux.

365 In all the experiments, it can be concluded that the shim+mesh configuration, which yields
366 the highest flux, achieved this elevated performance because of the shim's ability to deliver
367 larger amounts of heat to the system. However, the heat use efficiency, i.e., the efficiency at
368 which this heat is converted to vapor, was highest with the mesh-only configuration, which is
369 explored further below in Section 3.3. In all experiments and configurations, salt rejection was
370 higher than 99.9% throughout the entire experimental process.

371

372 ***3.3.*** **System energy performance**

373 When evaluating the system performance of an MD process, distillate flux is an important
374 criterion (used to determine the needed membrane area, and more generally the capital costs of
375 the system), but it is also critical to consider the energy needed to drive the process (typically, a
376 major component of the operating expenses). The energy performance of the system under
377 different operating conditions in terms of GOR and SEC was investigated. SEC is determined by
378 both energy consumption and distillate flux. Among the three operating variables, thermal
379 energy consumption is strongly associated with heat source temperature and is hardly affected by
380 cross-flow velocity and permeate pressure. In contrast, the electrical energy consumption is
381 dominated by the pumping rate (i.e., the cross-flow velocity) and vacuum pressure.

382 The impact of the heat source temperature (i.e., thermal energy input) on the system's SEC is
383 shown in Figs. 4a-4b. Specifically, in Fig. 4a, in the heat source temperature range of 140 °C to
384 420 °C, which corresponds to a total heat input to the system of ~3.8 W to ~13.9 W, the STEC

385 increased from 947 to 2449 kJ/kg. The results in Fig. 3b indicate that vapor flux increased with
386 increasing heat input; however, the flux increase rate was slower than the thermal energy input
387 increase rate. As a result, the cost of the elevated vapor flux with higher thermal energy input is
388 an increase in STEC. In contrast, in Fig. 4b, the flux increase rate was faster than the thermal
389 energy input increase rate, which leads to a decrease in STEC. However, at the same operating
390 temperature of 140 °C, STEC of shim-only configuration (3755 kJ/kg) is higher than that of
391 mesh-only configuration (947 kJ/kg); increasing the shim temperature beyond 140 °C was not
392 possible due to damage to the plastic membrane housing. This demonstrates that based on STEC,
393 mesh heating is more efficient than shim heating; under the given operating conditions, lower
394 thermal input is more favorable in terms of thermal energy efficiency, albeit with other costs
395 associated with lower flux operation (i.e., larger membrane surface area and capital cost to treat a
396 given volume of contaminated water). A decrease in SEEC was observed as the heat source
397 temperature increased simply because the flux (denominator) increased (Fig. 4a-4b). Electrical
398 energy consumption in the system is associated with the electricity needed to operate the vacuum
399 and circulation pumps, neither of which had changed substantially as the heat input increased.
400 Because STEC is approximately 3 orders of magnitude higher than SEEC, the net change of
401 STEC and SEEC (i.e., the overall SEC) increased as heat input to the system increased. For
402 example, the SEC value is approximately 2.5 times greater at 420 °C compared to 140 °C (heat
403 source temperature) for the mesh-only configuration.

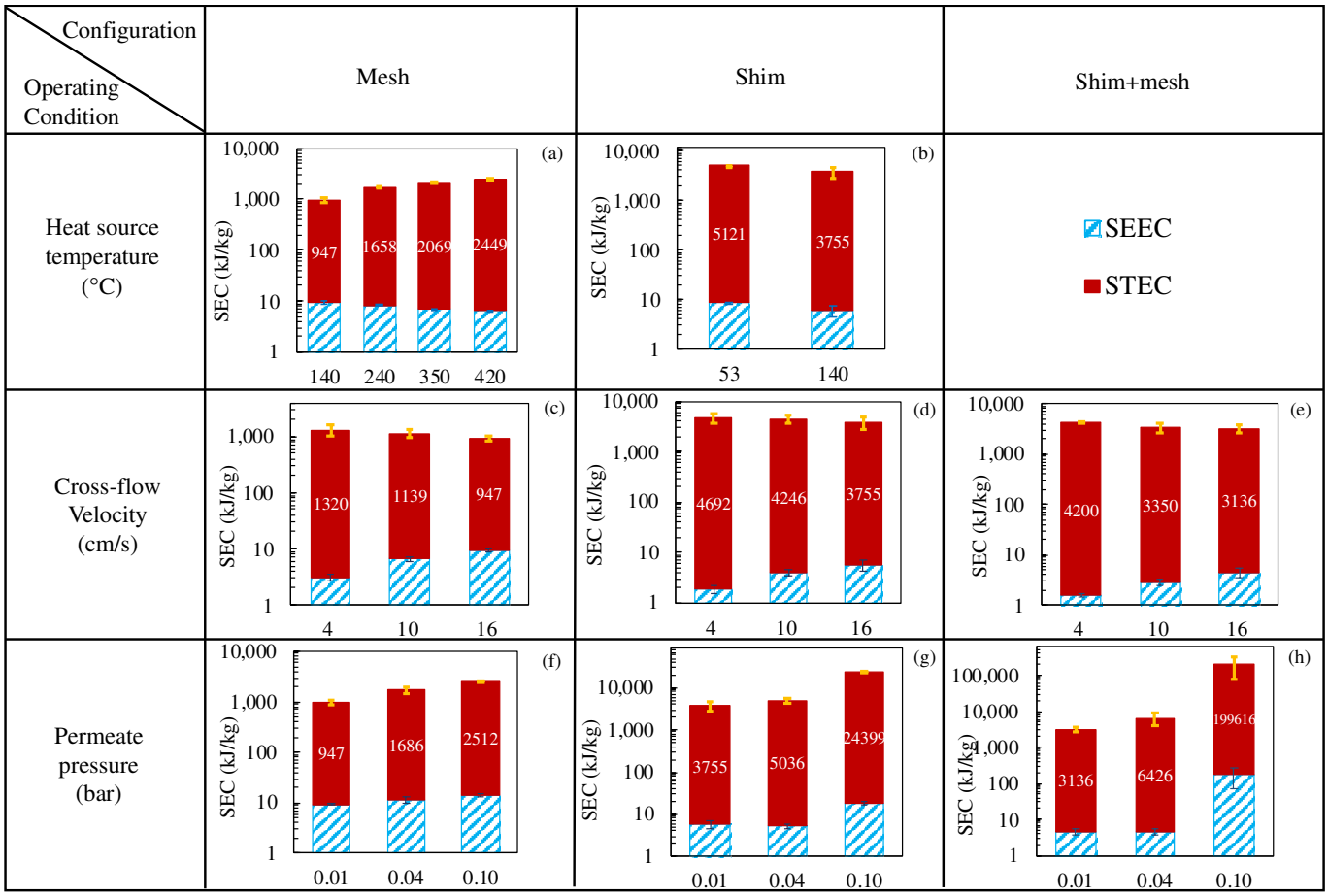

Fig. 4. SEC of 2h long vacuum membrane distillation tests with different system configurations as indicated in the figures: only shim in the feed stream, only mesh on the permeate side or both shim in the feed stream and mesh on the permeate side as the thermal carrier(s). All tests were performed with feed water contains 100 g/L NaCl. Regarding the operating conditions, unless specified as the variable, the heater temperature was set as 140 °C, cross-flow velocity was fixed at 16 cm/s and the permeate pressure was kept at 0.01 bar. The blue hatch bar represents the value of SEEC and the red solid bar represents the value of STEC. The SEC value is the sum of SEEC and STEC (the total bar height) as shown in the figures.

The effect of crossflow velocity on the system energy performance in terms of SEC are shown in Figs. 4c-4e. For all tested configurations, the overall SEC decreased with increasing crossflow velocity. When crossflow velocity increases, the thermal energy input to the system is not affected substantially, whereas there is a slight increase in electrical energy consumption from the recirculation pump. However, the addition of small amount of electrical energy input

417 (due to circulating the feed at a higher velocity) brought much higher flux as a benefit, which is
418 reflected in the SEC values. Overall, the SEC of the system was lowered by the increase in
419 crossflow velocity. Specifically, when the crossflow velocity increased from 4 to 16 cm/s, SEC
420 deceased by 26.5 ± 8.7 %, 20.5 ± 6.6 %, 25.3 ± 14.1 %, for the mesh, shim, and shim+mesh
421 configurations, respectively. Among the three configurations, the mesh-only configuration
422 showed the lowest SEC (947 to 1,320 kJ/kg depending on the crossflow velocity, with a flux
423 range of 2.6 to 3.5 LMH), followed by shim+mesh configuration (3,136 to 4,200 kJ/kg, with a
424 flux range of 5.3 to 7.6 LMH), and shim only configuration (3,735 to 4,692 kJ/kg, with a flux
425 range of 4.6 to 6.0 LMH). This demonstrates the advantage of providing heat directly to the
426 membrane surface in terms of minimizing specific energy consumption of the system, although
427 the most energy efficient system tends to deliver the least water flux.

428 Figs. 4(f) to 4(h) demonstrate the effects of the vacuum pressure on system SEC. For all
429 tested configurations, SEC increased with increasing permeate absolute pressure. While the
430 thermal energy input to the system was not affected when permeate pressure increased (i.e.,
431 vacuum depth decreases), the electrical energy required to induce vacuum should be lower when
432 the vacuum pump needs to maintain a lower vacuum. While the energy consumption did not
433 change much, the vapor flux decreased substantially when the permeate pressure was higher.
434 Thus, both STEC and SEEC increased substantially as a result of increase in permeate absolute
435 pressure. To achieve the lowest SEC (both STEC and SEEC) values and highest flux, the
436 pressure on the permeate side should be maintained as low as possible. Of the three
437 configurations tested, the mesh-only configuration exhibits the smallest SEC (947 to 2,512 kJ/kg)
438 with lowest flux (1.1 to 3.5 LMH). The shim+mesh configuration that generates the highest flux
439 (0.9 to 7.6 LMH) was the least energy efficient with a high SEC range of 3,136 to 199,616 kJ/kg.

Again, the results demonstrate the advantage of providing heat to the membrane surface, compared to heating the bulk stream in terms of energy efficiency, but with reduced water productivity.

The flux and energy performance of different MD systems, including data from this study (blue squares, grey triangles, and yellow circles) and others [17,23,39,47–65] (orange diamonds) are summarized in Fig. 5. As shown in Fig. 5, the 48 STEC values from cited references fluctuate substantially over 3 orders of magnitude. The broad range of STEC from different systems indicates that STEC is sensitive to system characteristics and operating parameters, which also implies a great potential for STEC improvement in most MD processes. In general, systems that include a surface heating element demonstrated the lower STEC values, which shows the important role that surface heating plays in increasing system energy efficiency [27,28]. It further stresses the importance of identifying the right location for incorporating the heat conducting element into a VMD system. Compared to other studies, the STEC values from this study are on the lower side. However, this low STEC is achieved at the cost of low flux. Note that the lowest STEC values in Fig. 5 have been recorded in surface heating (mesh only configuration) VMD settings with the water flux performance at the lower end (less than 5 LMH). When heat conducted through mesh is the only means of heat input, the thermal energy delivered to the system is limited and vacuum makes an important contribution to the generated flux. In these scenarios, a low thermal energy input could deliver reasonable flux with the assistance from the vacuum (i.e., increased electrical energy consumption), and the STEC values appear to be lower. When membrane heating was combined with bulk feed heating (the shim+mesh configuration), the flux is higher, but the SEC of the system increased. Flux is related to the membrane area needed to achieve a certain water treatment rate. Low flux systems,

by definition, require larger surface areas, which translates into higher capital costs. In contrast, the SEC (STEC as the major component) determines the operational cost of the system. Therefore, it is important to evaluate both flux performance and energy performance of a system and balance the tradeoff between membrane flux and SEC, to minimize the overall cost.

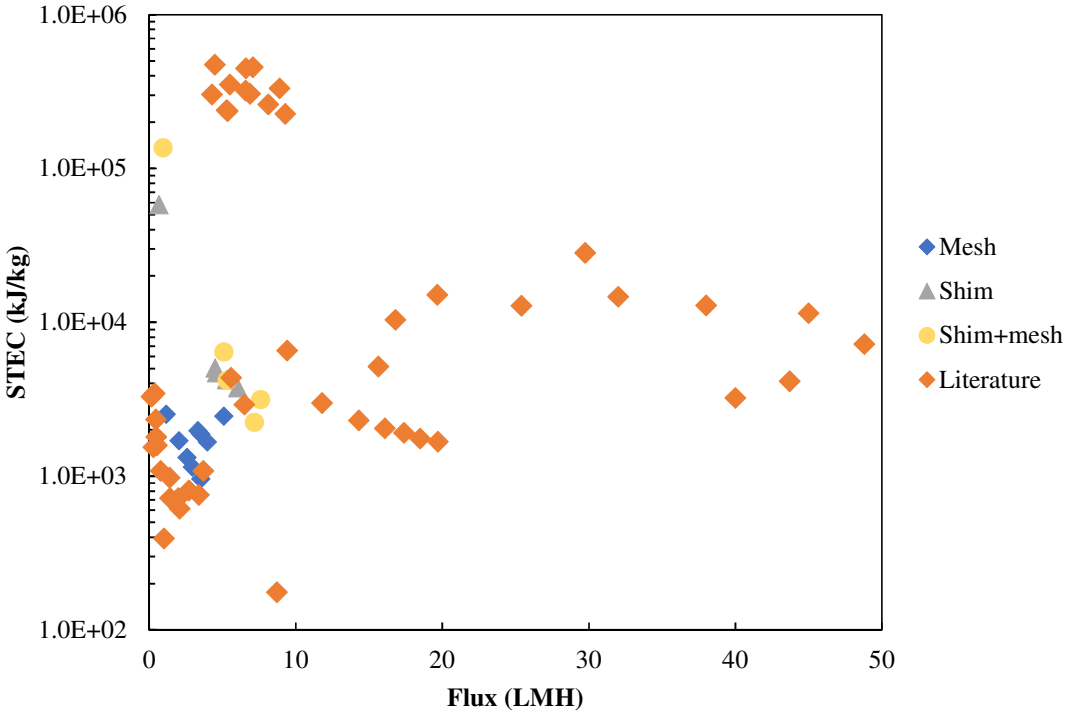

Fig. 5. Comparison of performance of different membrane distillation systems, including STEC (thermal energy performance) and flux (water productivity). Feed temperature data are available in Table S3 in SI. The orange diamonds represent the data from literature [17,23,54–63,39,64,65,47–53]. The blue squares, grey triangles and yellow circles represent the data from the direct heating MD experiments with mesh only configuration, shim only configuration, and shim+mesh configuration from this study, respectively. Higher flux indicates better water production and lower STEC values indicate higher thermal energy efficiency.

The direct heating MD system presented here is different from conventional MD systems where the driving force for desalination is delivered through the feed stream. When heat is delivered to where it is needed (i.e., the membrane/water interface), it only requires a minimal amount of thermal energy input because the heat at the interface can be more effectively used for evaporation, particularly with vacuum assistance. However, increased efficiency comes at a cost

of lower flux. Therefore, when considering the application of these systems, the efficiency of energy consumption must be balanced with increased capital expenses.

3.4. Numerical analysis

We complement our experimental measurements with a numerical model that simulates steady-state heat transport and vapor production in the VMD system sketched in Fig. 6. A feed channel of length L, height H, and width W is bounded by thermally insulated walls at $z = \pm W/2$ and $y = H$. The feed channel is bounded at $y = 0$ by a hydrophobic membrane of thickness δ_1, overlying a metallic mesh of thickness δ_2. We neglect concentration polarization, and assume pure water enters the channel at $x = 0$ with a uniform temperature T_{in} and mean velocity U_{in}.

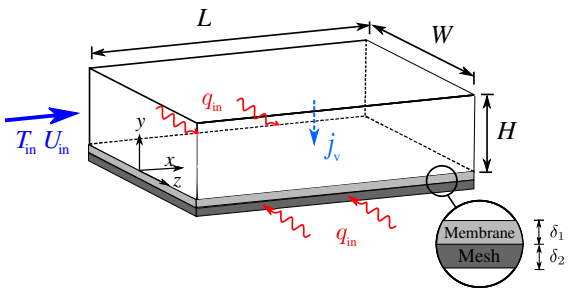

Fig. 6. Illustration (not to scale) of the geometry considered by our numerical analysis.

Steady heat transport in the channel is governed by the thermal energy equation,

$$\nabla \cdot (\mathbf{u}T) = \alpha_f \nabla^2 T \qquad (12)$$

where T, $\boldsymbol{u} = [u, v, w]$, and α_f are the feed temperature, velocity vector, and thermal diffusivity, respectively. We assume incompressible feed flow and neglect variations of α_f with temperature. We evaluate α_f using T_{in}. Though ongoing work in our group includes simulation of the Navier-Stokes equation in the feed channel, we present here a simpler model that approximates the feed velocity as

$$u(x,y,z) \approx u_d(y,z),\ v(x,y,z) \approx v_m(y,z),\ w = 0 \qquad (13)$$

where the downstream velocity $u_d(y,z)$ is the analytical solution for fully-developed laminar duct flow[66] , and $v_m(y,z)$ is the feed velocity normal to the membrane, evaluated at the membrane surface, $y = 0$. This approximation reduces CPU time and leverages the fact that v is typically four orders-of-magnitude smaller than U_{in}, such that downstream variations of $u(x,y,z)$ are very small. Furthermore, the membrane-normal velocity v primarily impacts heat transport in a thermal boundary-layer at the membrane surface. Satisfaction of the no-slip and no-penetration conditions for v on the impermeable walls is consequently of secondary importance. Note that our model captures variations of the feed temperature and vapor flux over the membrane surface.

We apply the following temperature boundary conditions in the feel channel,

$$T|_{x=0} = T_{in},\ \left.\frac{\partial T}{\partial z}\right|_{z=\pm W/2} = \left.\frac{\partial T}{\partial y}\right|_{y=h} = \left.\frac{\partial^2 T}{\partial x^2}\right|_{x=L} = 0 \qquad (14)$$

We model vapor transport through the composite membrane using the Schofield model [67], which assumes the transmembrane mass flux j satisfies Eq. 10 where the vapor pressure $P_{m,f}$ at the membrane feed surface ($y = 0$) is computed using Eq. 11.

As detailed in Section S5 in the Supporting Information, heat transport in the membrane and mesh layers can be modeled using the volume-averaged equation,

$$\frac{\partial}{\partial y}\left(T c_{p,v} j_v\right) = k_i \nabla^2 T, \qquad k_i = \phi_i k_v + (1-\phi_i) k_{s,i} \qquad (15)$$

where $c_{p,v}$ is the specific heat at constant pressure of the vapor, k_i is an effective thermal conductivity, ϕ_i is the porosity, and k_v and $k_{s,i}$ are the thermal conductivities of the vapor and solid phases, respectively. The subscript $i = 1, 2$ is used to distinguish between the properties evaluated in the membrane layer ($i = 1$) or underlying mesh ($i = 2$).

Conservation of energy [68] requires the following conditions at the feed-membrane interface,

$$T|_{y=0^+} = T|_{y=0^-}, \qquad k_f \left.\frac{\partial T}{\partial y}\right|_{y=0^+} - k_1 \left.\frac{\partial T}{\partial y}\right|_{y=0^-} = j\lambda \tag{16}$$

where λ = -2,438T + 250,300 is the latent heat of water vaporization, assuming T and λ have units °C and kJ/kg, respectively. This relation was derived using the OLI Stream Analyzer database. The superscripts + and - denote evaluation of T at the feed and membrane side of the interface, respectively. Conservation of energy at the interface between the membrane and mesh requires,

$$T|_{y=\delta_1^+} = T|_{y=\delta_1^-}, \; k_1 \left.\frac{\partial T}{\partial y}\right|_{y=\delta_1^+} = k_2 \left.\frac{\partial T}{\partial y}\right|_{y=\delta_1^-} \tag{17}$$

On the inlet, outlet, and lower surface of the composite membrane, we assume negligible conductive heat transport,

$$\left.\frac{\partial T}{\partial x}\right|_{x=0} = \left.\frac{\partial T}{\partial x}\right|_{x=L} = \left.\frac{\partial T}{\partial y}\right|_{y=-\delta_1-\delta_2} = 0 \tag{18}$$

Note that thermal energy nevertheless exits the system through the membrane due to advection. On the side walls $z = \pm W/2$, we assume the membrane layer is thermally insulated,

$$\left.\frac{\partial T}{\partial z}\right|_{z=\pm W/2} = 0, \; -\delta_1 < y < 0 \tag{19}$$

while heat enters the system through the mesh,

$$k_2 \left.\frac{\partial T}{\partial z}\right|_{z=\pm W/2} = q_{in}, \; -\delta_1 - \delta_2 < y \leq -\delta_1 \tag{20}$$

All equations are discretized spatially using second-order finite-volume methods coded in-house with Fortran [69,70]. The code was verified against analytical solutions and validated against experimental data, as detailed in Dudley [71] and demonstrated by Lou *et al.* [70]. We also performed mesh-independence studies to ensure a relative truncation error on the order of 1 %. Fig. 7 demonstrates our validation, in which we compare the vapor flux predictions of our model to those measured by our bench-scale system. For that purpose, we set the model

dimensions (L = 10 cm, W = 4 cm, and H = 4 mm), membrane properties (ϕ_1 = 0.85, δ_1 = 100 μm, $k_{s,1}$ = 0.11 W/m-K), and mesh properties (ϕ_2 = 0.27, δ_2 = 203.2 μm, $k_{s,2}$ = 200 W/m-K) to those of the experimental system. Note that the thermal conductivities of the membrane and mesh are set to those of polypropylene and aluminum, respectively. We also modified the numerical model to apply heat to only side of the membrane, consistent with experiments. Experiments and simulations were then performed for the combinations of heat inputs q_{in}, inlet temperatures T_{in}, and flow rates U_{in} summarized in Table 1, for the constant vacuum pressure P_{vac} = 0.01 bar. As heat input can vary depending on the thermal conducting layer material and dimension, the heat source type and temperature, and system configuration, the heat input q_{in} was chosen as a normalizing factor in the simulation studies. The flow was heated using only the mesh, i.e. without the heated shim.

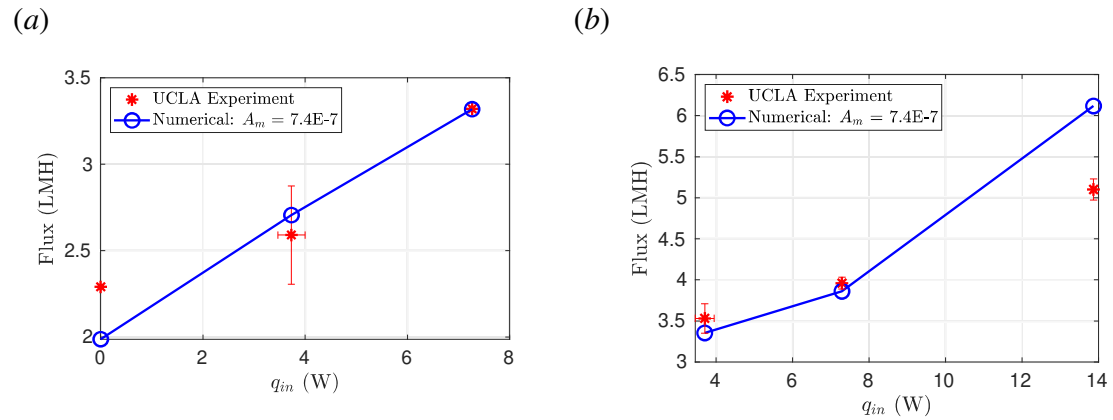

Fig. 7. Comparison of experimental (red asterisks) and numerical (blue circles) measurements of vapor flux as a function of q_{in} for (a) experiments labeled 1-3 in Table 1, (b) experiments labeled 4-6 in Table 1.

Table 1. Operating conditions used for experiments and simulations presented in Fig. 7.

Exp #	**1**	**2**	**3**	**4**	**5**	**6**
q_{in} (W)	0	3.73	7.26	3.70	7.29	13.9
T_{in} (°C)	16.8	18.4	19.5	20.2	21.0	25.7
U_{in} (cm/s)	4.06	4.06	4.06	16.3	16.3	16.3

559 Fig. 7(*a*) compares our experimental (red asterisks) and numerical (blue circles) results for
560 the average transmembrane vapor flux as a function of q_{in} for the experiments labeled 1-3 in
561 Table 1. These were conducted for the relatively slow feed velocity U_{in} = 4.06 cm/s. Note the
562 reported value of T_{in} from Table 1 represents the average feed temperature throughout the entire
563 experiment; the increase in T_{in} with q_{in} is explained by the recycling of the concentrate in the
564 experimental system. The only model parameter not known *a-priori* is the membrane vapor
565 permeability A_m. For that purpose, we performed a large suite of simulations for different values
566 of A_m, and found that A_m = 7.4 x 10^{-7} kg/m s Pa provided the best fit to the experimental data in
567 Fig. 7(*a*), producing a mean percentage error of 5.9%. This permeability is roughly 25% lower
568 than those reported by Vanneste *et al*. [72] and Lou *et al*. [70], who report A_m = 10^{-6} and 1.87 x
569 10^{-6} kg/m·s·Pa, respectively, for the same membrane material in a direct contact MD system.
570 The difference likely arises because our permeability is an effective value for both the membrane
571 and underlying mesh material. Having determined A_m, we then compared experimental and
572 numerical results for the experiments labeled 4-6 in Table 1, which were performed for the larger
573 feed velocity U_{in} = 16.3 cm/s. Fig. 7(*b*) shows that in this case, our model agrees with the
574 experiments to within 9.2 % mean percentage error. An additional validation of our numerical
575 model for cases with a heated shim are provided in Supporting Information (Section S6). With
576 the successful model validation using experimental results from different operational conditions,
577 parametric studies were performed to predict system performance in a larger-scale flow cell.
578 These simulation results serve as guidance of the optimization of operational conditions in a
579 scaled-up system with minimal experiments.

580 To explore heat transport and vapor production in a larger VMD system, we perform a
581 parametric study for a system of dimensions L = 1 m, W = 8 cm, and h = 2 mm and a constant

582 inlet feed temperature of T_{in} = 30 °C. We assume that vacuum evacuates all the vapor and
583 maintains a constant driving force on the permeate side. All properties of the composite
584 membrane were set to those of the experimental system, with the exception of the mesh thickness,
585 which was rounded down to δ_2 = 200 μm. We then varied the heat input between $0 \leq q_{in} \leq 400$ W,
586 considering a larger system might require higher heat input compared to the bench-scale system.
587 We studied the feed velocity between $1 \leq U_{in} \leq 10$ cm/s, which is a practical velocity range
588 during membrane operations – high enough to contribute to membrane fouling control, but not
589 too high so as to substantially increase operational costs. Heat was applied to both lateral edges
590 of the mesh, i.e. at $z = \pm W/2$.

591 To investigate the impact of mesh heating (q_{in}), we begin by setting U_{in} = 10 cm/s and q_{in} =
592 20 W. Fig. 8(*a*) shows the resulting cross-sectional temperature profiles on the membrane
593 surface (y = 0) at the downstream locations $x = L/4$ (solid line), $L/2$ (dashed line), and L (dash-
594 dotted line). The highest temperatures occur near the lateral walls, where the heating is applied.
595 For this small value of q_{in}, we see that the maximum temperature is always below the inlet value,
596 T_{in} = 30 °C, and also decreases with downstream distance. This occurs because the low heat
597 input does not match that lost to evaporation. Fig. 8(*b*) shows the corresponding results when the
598 heating is increased to q_{in} = 400 W. The maximum temperature is now always above the inlet
599 value, reaching T = 55 °C at the outlet. The maximum temperature also increases with
600 downstream distance. Meanwhile, the lowest membrane temperatures occur in the middle of the
601 membrane, and remain near the inlet value T_{in} = 30 °C. We conclude that for this high heating
602 value, q_{in} exceeds the heat lost to evaporation, such that temperature polarization is not only
603 removed, but actually reversed. We also observe that the temperature profiles suddenly flatten

near the lateral walls at $z = \pm W/2$. This is an artifact of our discretization of the thermally insulated boundary conditions.

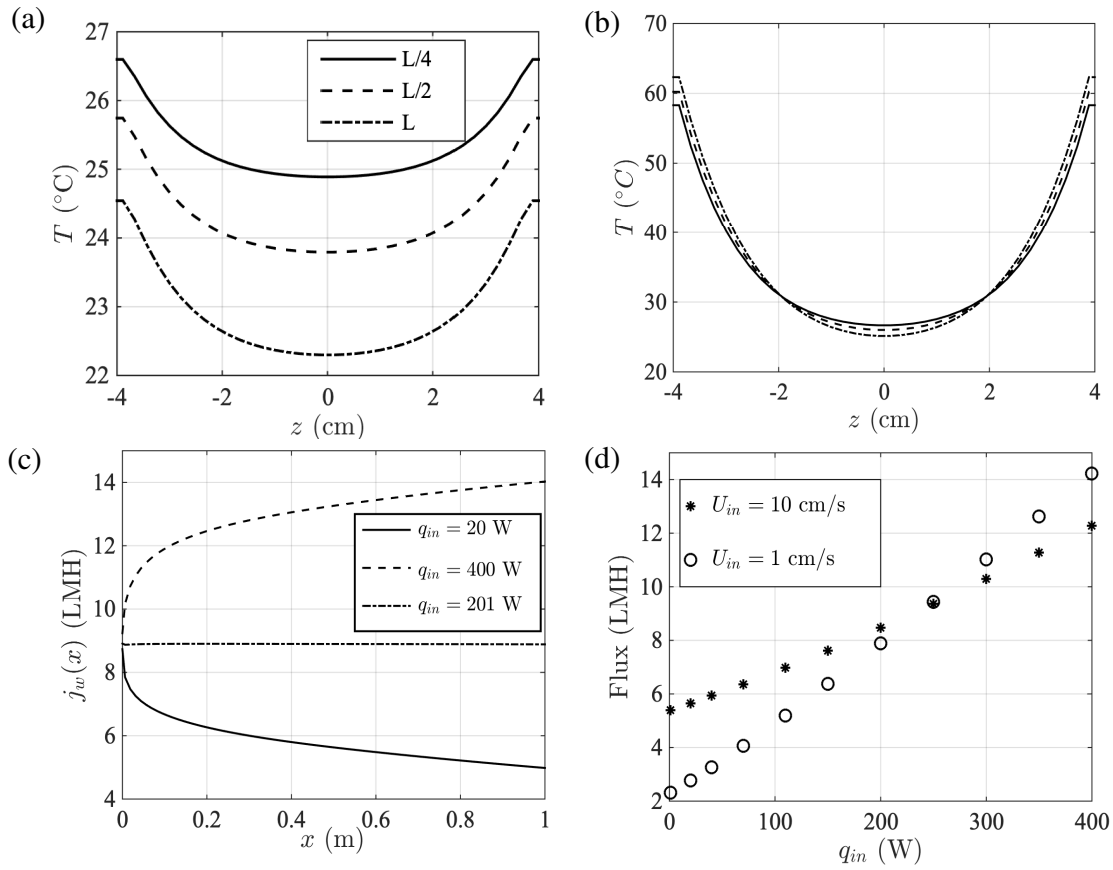

Fig. 8. (a) Temperature profiles on the membrane surface ($y = 0$) at the downstream locations $x = L/4$ (solid line), $L/2$ (dashed line), and L (dash-dotted line) when $q_{in} = 20$ W and $U_{in} = 10$ cm/s. (*b*) Corresponding temperature profiles when $q_{in} = 400$ W and $U_{in} = 10$ cm/s. (c) Downstream variation of the width-averaged flux $j_w(x)$ when $U_{in} = 10$ cm/s and $q_{in} = 20$ W (solid line), $q_{in} = 400$ W (dashed line), and $q_{in} = 201$ W (dashed-dotted line). (*d*) Net flux as a function of q_{in} when $U_{in} = 10$ cm/s (asterisk symbols) and $U_{in} = 1$ cm/s (circles).

To explore the impact of heating on local vapor production, we define the width-averaged flux

$$j_w(x) = \frac{1}{W}\int_{-W/2}^{W/2} j_v(x,z)\, dz \qquad (22)$$

Fig. 8(*c*) shows the downstream variation of $j_w(x)$ when $U_{in} = 10$ cm/s and $q_{in} = 20$ W (solid line) and $q_{in} = 400$ W (dashed line). We see that for $q_{in} = 20$ W, the vapor flux decreases with

618 downstream distance due to temperature polarization. In contrast, when q_{in} = 400 W, we see $j_w(x)$
619 increases with downstream distance. An additional series of simulations found that when q_{in} =
620 201 W, the width-averaged flux j_w (x) is constant, as demonstrated by the dash-dotted line in Fig.
621 8(c). For active heating above this threshold value, the single-pass recovery of the heated VMD
622 system can be increased by simply increasing the system length, without suffering from
623 downstream heat loss due to temperature polarization.

624 Fig. 8(*d*) shows the net vapor flux as a function of q_{in} when U_{in} = 10 cm/s (asterisks) and U_{in}
625 = 1 cm/s (circles). We see that for heating values below around q_{in} = 250 W, the higher feed
626 velocity produces more net flux. That occurs because the heating is not sufficient to completely
627 reverse the effects of temperature polarization. In that case, a higher feed velocity is preferred,
628 because it reduces the impact of temperature polarization, and increases the net flux. This likely
629 explains our experimental observations that distillate flux increased with feed velocity. In
630 contrast, for heating values above q_{in} = 250 W, the lower feed velocity produces more flux. In
631 this case, a lower feed velocity increases the residence time of the feed passing through the
632 channel, and allows it to heat to higher values, thereby increasing flux. When treating feed
633 waters for which mineral scaling is not a concern, we conclude that systems can benefit from
634 operating at a high q_{in} and a low U_{in}. For the case of high-concentration brines, one must also
635 consider that lower feed velocities tend to exacerbate concentration polarization and mineral
636 scaling.

637 We have demonstrated experimentally and numerically that the direct heating approach is
638 capable of mitigating or even reversing temperature polarization. It is important to note that
639 temperature and concentration polarization are coupled phenomena because they both depend on,
640 and influence the water vapor flux through the membrane. On the one hand, the elevated

membrane surface temperature helps to maximize vapor flux by maintaining the driving force and reduce some scaling by increasing the solubility of alkali metal salts (e.g., NaCl). On the other hand, high temperatures at the membrane/water interface increases vapor flux, which increases concentration polarization and reduces the solubility of certain common mineral species (e.g., $CaCO_3$ and $CaSO_4$), which increases scaling. Therefore, temperature polarization needs to be optimized to an appropriate level where flux is maximized while scaling is minimized (or at the very least kept at a tolerable level).

4. Conclusions

We developed a VMD process using layered composite membranes that include a high-thermal-conductivity layer for supplying heat directly to the membrane-water interface and throughout the flow channel. The VMD system showed stable performance over hours of desalinating hypersaline feed and exhibited water fluxes as high as 9 LMH and salt rejection >99.9%. We also investigated the impact of operational conditions on system performance. Flux was shown to be affected by heat input, feed crossflow velocity, and vacuum level, while salt rejection remained to be higher than 99.9% under all the tested conditions. Our CFD simulations were in agreement with experimental results. The numerical models developed here were able to successfully describe the transport phenomena in the system and predict the ability to use this VMD process for larger scale systems. Compared to conventional VMD systems, direct heating VMD systems demonstrated higher energy efficiency, which stresses the importance of identifying the right location for incorporating the heat conducting element into a VMD system. This process has the potential of solving several problems associated with MD-

663 based desalination and brine concentration processes, such as minimizing heat losses, increasing
664 thermal efficiency, and limiting the number of heat exchangers.
665
666 **Credit authorship contribution statement**
667 **Jingbo Wang:** Investigation, Data curation, Methodology, Visualization, Writing - original draft.
668 **Yiming Liu:** Investigation, Data curation, Writing - review & editing.
669 **Unnati Rao:** Investigation.
670 **Mark Dudley:** Investigation, Data curation, Methodology, Visualization, Writing - original draft.
671 **Navid Dehdari Ebrahimib:** Investigation, Methodology.
672 **Jincheng Lou:** Investigation.
673 **Fei Han:** Investigation.
674 **Eric M.V. Hoek:** Supervision, Writing - review & editing.
675 **Nils Tilton:** Supervision, Writing - review & editing.
676 **Tzahi Y. Cath:** Supervision, Writing - review & editing.
677 **Craig S. Turchi:** Supervision, Writing - review & editing.
678 **Michael B. Heeley:** Supervision, Writing - review & editing.
679 **Y. Sungtaek Ju:** Methodology.
680 **David Jassby:** Funding acquisition, Methodology, Supervision, Conceptualization, Writing -
681 review & editing
682
683 **Acknowledgements**

The SEM and EDAX analyses were conducted at the California NanoSystems Institute, Los Angeles, California, 90095, USA. This work was supported by the Department of Energy (DOE) (Award No. DE-EE0008391) and the Sustainable LA Grand Challenge (EMVH).

Supporting information

Additional experimental details are provided including:

- Section S1. Thermal conductivity measurement of thermal carriers
- Section S2. Temperature profile on the surface of thermal carriers
- Section S3. Characterization of metal components of the direct heating VMD system
- Section S4. System energy performance - GOR
- Section S5. Heat transport model derivation
- Section S6. Additional model validation with experimental results
- Section S7. Additional details of the VMD experiments
- Section S8. Feed temperature summary from literature and this study

References cited

[1] M.S. El-Bourawi, Z. Ding, R. Ma, M. Khayet, A framework for better understanding membrane distillation separation process, J. Membr. Sci. (2006). https://doi.org/10.1016/j.memsci.2006.08.002.

[2] K.W. Lawson, D.R. Lloyd, Membrane distillation, J. Membr. Sci. (1997). https://doi.org/10.1016/S0376-7388(96)00236-0.

[3] A. Alkhudhiri, N. Darwish, N. Hilal, Membrane distillation: A comprehensive review, Desalination. 287 (2012) 2–18. https://doi.org/10.1016/j.desal.2011.08.027.

[4] J. Wu, K.R. Zodrow, P.B. Szemraj, Q. Li, Photothermal nanocomposite membranes for direct solar membrane distillation, J. Mater. Chem. A. 5 (2017) 23712–23719. https://doi.org/10.1039/c7ta04555g.

[5] X. Chen, N.Y. Yip, Unlocking High-Salinity Desalination with Cascading Osmotically Mediated Reverse Osmosis: Energy and Operating Pressure Analysis, Environ. Sci. Technol. (2018). https://doi.org/10.1021/acs.est.7b05774.

[6] C.K. Chiam, R. Sarbatly, Vacuum membrane distillation processes for aqueous solution treatment-A review, Chem. Eng. Process. - Process Intensif. 74 (2013) 27–54. https://doi.org/10.1016/j.cep.2013.10.002.

[7] M.A.E.R. Abu-Zeid, Y. Zhang, H. Dong, L. Zhang, H.L. Chen, L. Hou, A comprehensive review of vacuum membrane distillation technique, Desalination. 356 (2015) 1–14. https://doi.org/10.1016/j.desal.2014.10.033.

[8] S. Lin, N.Y. Yip, M. Elimelech, Direct contact membrane distillation with heat recovery: Thermodynamic insights from module scale modeling, J. Membr. Sci. (2014). https://doi.org/10.1016/j.memsci.2013.11.016.

[9] M. Qtaishat, T. Matsuura, B. Kruczek, M. Khayet, Heat and mass transfer analysis in direct contact membrane distillation, Desalination. (2008). https://doi.org/10.1016/j.desal.2007.05.019.

[10] A.S. Alsaadi, L. Francis, G.L. Amy, N. Ghaffour, Experimental and theoretical analyses of temperature polarization effect in vacuum membrane distillation, J. Membr. Sci. 471 (2014) 138–148. https://doi.org/10.1016/j.memsci.2014.08.005.

[11] G. Zuo, G. Guan, R. Wang, Numerical modeling and optimization of vacuum membrane distillation module for low-cost water production, Desalination. 339 (2014) 1–9. https://doi.org/10.1016/j.desal.2014.02.005.

[12] J.P. Mericq, S. Laborie, C. Cabassud, Vacuum membrane distillation of seawater reverse osmosis brines, Water Res. 44 (2010) 5260–5273. https://doi.org/10.1016/j.watres.2010.06.052.

[13] S. Bandini, C. Gostoli, G.C. Sarti, Separation efficiency in vacuum membrane distillation, J. Membr. Sci. (1992). https://doi.org/10.1016/0376-7388(92)80131-3.

[14] S.G. Lovineh, M. Asghari, B. Rajaei, Numerical simulation and theoretical study on simultaneous effects of operating parameters in vacuum membrane distillation, Desalination. (2013). https://doi.org/10.1016/j.desal.2013.01.005.

[15] J. Zhang, J. De Li, M. Duke, M. Hoang, Z. Xie, A. Groth, C. Tun, S. Gray, Modelling of vacuum membrane distillation, J. Membr. Sci. 434 (2013) 1–9. https://doi.org/10.1016/j.memsci.2013.01.048.

[16] M. Khayet, Solar desalination by membrane distillation: Dispersion in energy consumption analysis and water production costs (a review), Desalination. 308 (2013) 89–101. https://doi.org/10.1016/j.desal.2012.07.010.

[17] A. Deshmukh, C. Boo, V. Karanikola, S. Lin, A.P. Straub, T. Tong, D.M. Warsinger, M. Elimelech, Membrane distillation at the water-energy nexus: Limits, opportunities, and challenges, Energy Environ. Sci. 11 (2018) 1177–1196. https://doi.org/10.1039/c8ee00291f.

[18] Y. Zhou, R.S.J. Tol, Evaluating the costs of desalination and water transport, Water Resour. Res. (2005). https://doi.org/10.1029/2004WR003749.

[19] M. Shannon, P.W. Bohn, M. Elimelech, J.G. Georgiadis, B.J. Mariñas, A.M. Mayes, Science and technology for water purification in the coming decades, Nature. 452 (2008) 301–310. https://doi.org/10.1038/nature06599.

[20] P.A. Hogan, Sudjito, A.G. Fane, G.L. Morrison, Desalination by solar heated membrane distillation, Desalination. (1991). https://doi.org/10.1016/0011-9164(91)85047-X.

[21] F. Banat, R. Jumah, M. Garaibeh, Exploitation of solar energy collected by solar stills for desalination by membrane distillation, Renew. Energy. (2002). https://doi.org/10.1016/S0960-1481(01)00058-1.

[22] J. Koschikowski, M. Wieghaus, M. Rommel, Solar thermal-driven desalination plants based on membrane distillation, Desalination. (2003). https://doi.org/10.1016/S0011-9164(03)00360-6.

[23] J. Koschikowski, M. Wieghaus, M. Rommel, V.S. Ortin, B.P. Suarez, J.R. Betancort Rodríguez, Experimental investigations on solar driven stand-alone membrane distillation systems for remote areas, Desalination. (2009). https://doi.org/10.1016/j.desal.2008.05.047.

[24] F. Banat, N. Jwaied, M. Rommel, J. Koschikowski, M. Wieghaus, Performance evaluation of the “large SMADES” autonomous desalination solar-driven membrane distillation plant in Aqaba, Jordan, Desalination. 217 (2007) 17–28. https://doi.org/10.1016/j.desal.2006.11.027.

[25] J. Blanco Gálvez, L. García-Rodríguez, I. Martín-Mateos, Seawater desalination by an innovative solar-powered membrane distillation system: the MEDESOL project, Desalination. 246 (2009) 567–576. https://doi.org/10.1016/j.desal.2008.12.005.

[26] J.P. Mericq, S. Laborie, C. Cabassud, Evaluation of systems coupling vacuum membrane

774 distillation and solar energy for seawater desalination, Chem. Eng. J. (2011).
775 https://doi.org/10.1016/j.cej.2010.11.030.

776 [27] C. Chen, Y. Kuang, L. Hu, Challenges and Opportunities for Solar Evaporation, Joule.
777 (2019). https://doi.org/10.1016/j.joule.2018.12.023.

778 [28] L. Cui, P. Zhang, Y. Xiao, Y. Liang, H. Liang, Z. Cheng, L. Qu, High Rate Production of
779 Clean Water Based on the Combined Photo-Electro-Thermal Effect of Graphene
780 Architecture, Adv. Mater. (2018). https://doi.org/10.1002/adma.201706805.

781 [29] P.D. Dongare, A. Alabastri, S. Pedersen, K.R. Zodrow, N.J. Hogan, O. Neumann, J. Wud,
782 T. Wang, A. Deshmukh, M. Elimelech, Q. Li, P. Nordlander, N.J. Halas, Nanophotonics-
783 enabled solar membrane distillation for off-grid water purification, Proc. Natl. Acad. Sci.
784 U. S. A. (2017). https://doi.org/10.1073/pnas.1701835114.

785 [30] L. Huang, J. Pei, H. Jiang, X. Hu, Water desalination under one sun using graphene-based
786 material modified PTFE membrane, Desalination. (2018).
787 https://doi.org/10.1016/j.desal.2018.05.006.

788 [31] X. Han, W. Wang, K. Zuo, L. Chen, L. Yuan, J. Liang, Q. Li, P.M. Ajayan, Y. Zhao, J.
789 Lou, Bio-derived ultrathin membrane for solar driven water purification, Nano Energy.
790 (2019). https://doi.org/10.1016/j.nanoen.2019.03.089.

791 [32] B. Gong, H. Yang, S. Wu, G. Xiong, J. Yan, K. Cen, Z. Bo, K. Ostrikov, Graphene Array-
792 Based Anti-fouling Solar Vapour Gap Membrane Distillation with High Energy
793 Efficiency, Nano-Micro Lett. (2019). https://doi.org/10.1007/s40820-019-0281-1.

794 [33] S. Cao, X. Wu, Y. Zhu, R. Gupta, A. Tan, Z. Wang, Y.S. Jun, S. Singamaneni,
795 Polydopamine/hydroxyapatite nanowire-based bilayered membrane for photothermal-
796 driven membrane distillation, J. Mater. Chem. A. (2020).
797 https://doi.org/10.1039/c9ta12703h.

798 [34] I.A. Said, S. Wang, Q. Li, Field Demonstration of a Nanophotonics-Enabled Solar
799 Membrane Distillation Reactor for Desalination, Ind. Eng. Chem. Res. (2019).
800 https://doi.org/10.1021/acs.iecr.9b03246.

801 [35] L. Song, Q. Huang, Y. Huang, R. Bi, C. Xiao, An electro-thermal braid-reinforced PVDF
802 hollow fiber membrane for vacuum membrane distillation, J. Membr. Sci. 591 (2019)
803 117359. https://doi.org/10.1016/j.memsci.2019.117359.

804 [36] A. V. Dudchenko, C. Chen, A. Cardenas, J. Rolf, D. Jassby, Frequency-dependent
805 stability of CNT Joule heaters in ionizable media and desalination processes, Nat.
806 Nanotechnol. 12 (2017) 557–563. https://doi.org/10.1038/nnano.2017.102.

807 [37] O.R. Lokare, S. Tavakkoli, V. Khanna, R.D. Vidic, Importance of feed recirculation for
808 the overall energy consumption in membrane distillation systems, Desalination. (2018).
809 https://doi.org/10.1016/j.desal.2017.11.037.

810 [38] E. Deniz, S. Çınar, Energy, exergy, economic and environmental (4E) analysis of a solar
811 desalination system with humidification-dehumidification, Energy Convers. Manag.

(2016). https://doi.org/10.1016/j.enconman.2016.07.064.

[39] R. Miladi, N. Frikha, A. Kheiri, S. Gabsi, Energetic performance analysis of seawater desalination with a solar membrane distillation, Energy Convers. Manag. 185 (2019) 143–154. https://doi.org/10.1016/j.enconman.2019.02.011.

[40] M.I. Soomro, W.S. Kim, Performance and economic investigations of solar power tower plant integrated with direct contact membrane distillation system, Energy Convers. Manag. (2018). https://doi.org/10.1016/j.enconman.2018.08.056.

[41] A. Luo, N. Lior, Critical review of membrane distillation performance criteria, Desalin. Water Treat. 57 (2016) 20093–20140. https://doi.org/10.1080/19443994.2016.1152637.

[42] W.L. McCabe, J.C. Smith, P. Harriott, Unit Operations of Chemical Engineering, 4th ed., McGraw-Hill, New York, 1985.

[43] L. Kumar, M. Hasanuzzaman, N.A. Rahim, Global advancement of solar thermal energy technologies for industrial process heat and its future prospects: A review, Energy Convers. Manag. (2019). https://doi.org/10.1016/j.enconman.2019.05.081.

[44] A.A. Hachicha, B.A.A. Yousef, Z. Said, I. Rodríguez, A review study on the modeling of high-temperature solar thermal collector systems, Renew. Sustain. Energy Rev. (2019). https://doi.org/10.1016/j.rser.2019.05.056.

[45] M. Gryta, Effectiveness of water desalination by membrane distillation process, Membranes (Basel). (2012). https://doi.org/10.3390/membranes2030415.

[46] S.O. Olatunji, L.M. Camacho, Heat and mass transport in modeling membrane distillation configurations: A review, Front. Energy Res. 6 (2018) 1–18. https://doi.org/10.3389/fenrg.2018.00130.

[47] F. Banat, N. Jwaied, M. Rommel, J. Koschikowski, M. Wieghaus, Desalination by a "compact SMADES" autonomous solarpowered membrane distillation unit, Desalination. 217 (2007) 29–37. https://doi.org/10.1016/j.desal.2006.11.028.

[48] H.E.S. Fath, S.M. Elsherbiny, A.A. Hassan, M. Rommel, M. Wieghaus, J. Koschikowski, M. Vatansever, PV and thermally driven small-scale, stand-alone solar desalination systems with very low maintenance needs, Desalination. 225 (2008) 58–69. https://doi.org/10.1016/j.desal.2006.11.029.

[49] A. Criscuoli, M.C. Carnevale, E. Drioli, Evaluation of energy requirements in membrane distillation, Chem. Eng. Process. Process Intensif. 47 (2008) 1098–1105. https://doi.org/10.1016/j.cep.2007.03.006.

[50] X. Wang, L. Zhang, H. Yang, H. Chen, Feasibility research of potable water production via solar-heated hollow fiber membrane distillation system, Desalination. 247 (2009) 403–411. https://doi.org/10.1016/j.desal.2008.10.008.

[51] A. Ruiz-Aguirre, J.A. Andrés-Mañas, J.M. Fernández-Sevilla, G. Zaragoza, Experimental characterization and optimization of multi-channel spiral wound air gap membrane

distillation modules for seawater desalination, Sep. Purif. Technol. (2018). https://doi.org/10.1016/j.seppur.2018.05.044.

[52] G. Zaragoza, A. Ruiz-Aguirre, E. Guillén-Burrieza, Efficiency in the use of solar thermal energy of small membrane desalination systems for decentralized water production, Appl. Energy. (2014). https://doi.org/10.1016/j.apenergy.2014.02.024.

[53] H.C. Duong, A.R. Chivas, B. Nelemans, M. Duke, S. Gray, T.Y. Cath, L.D. Nghiem, Treatment of RO brine from CSG produced water by spiral-wound air gap membrane distillation - A pilot study, Desalination. (2015). https://doi.org/10.1016/j.desal.2014.10.026.

[54] R. Schwantes, A. Cipollina, F. Gross, J. Koschikowski, D. Pfeifle, M. Rolletschek, V. Subiela, Membrane distillation: Solar and waste heat driven demonstration plants for desalination, Desalination. (2013). https://doi.org/10.1016/j.desal.2013.04.011.

[55] A. Ruiz-Aguirre, J.A. Andrés-Mañas, J.M. Fernández-Sevilla, G. Zaragoza, Modeling and optimization of a commercial permeate gap spiral wound membrane distillation module for seawater desalination, Desalination. (2017). https://doi.org/10.1016/j.desal.2017.06.019.

[56] J.A. Andrés-Mañas, A. Ruiz-Aguirre, F.G. Acién, G. Zaragoza, Performance increase of membrane distillation pilot scale modules operating in vacuum-enhanced air-gap configuration, Desalination. (2020). https://doi.org/10.1016/j.desal.2019.114202.

[57] R.G. Raluy, R. Schwantes, V.J. Subiela, B. Peñate, G. Melián, J.R. Betancort, Operational experience of a solar membrane distillation demonstration plant in Pozo Izquierdo-Gran Canaria Island (Spain), Desalination. (2012). https://doi.org/10.1016/j.desal.2012.01.003.

[58] M. Li, K.J. Lu, L. Wang, X. Zhang, T.S. Chung, Janus membranes with asymmetric wettability via a layer-by-layer coating strategy for robust membrane distillation, J. Membr. Sci. (2020). https://doi.org/10.1016/j.memsci.2020.118031.

[59] E. Guillén-Burrieza, J. Blanco, G. Zaragoza, D.C. Alarcón, P. Palenzuela, M. Ibarra, W. Gernjak, Experimental analysis of an air gap membrane distillation solar desalination pilot system, J. Membr. Sci. 379 (2011) 386–396. https://doi.org/10.1016/j.memsci.2011.06.009.

[60] R. Sarbatly, C.K. Chiam, Evaluation of geothermal energy in desalination by vacuum membrane distillation, Appl. Energy. 112 (2013) 737–746. https://doi.org/10.1016/j.apenergy.2012.12.028.

[61] C. Cabassud, D. Wirth, Membrane distillation for water desalination: How to chose an appropriate membrane?, Desalination. 157 (2003) 307–314. https://doi.org/10.1016/S0011-9164(03)00410-7.

[62] W.G. Shim, K. He, S. Gray, I.S. Moon, Solar energy assisted direct contact membrane distillation (DCMD) process for seawater desalination, Sep. Purif. Technol. 143 (2015) 94–104. https://doi.org/10.1016/j.seppur.2015.01.028.

[63] Q. Ma, A. Ahmadi, C. Cabassud, Direct integration of a vacuum membrane distillation module within a solar collector for small-scale units adapted to seawater desalination in remote places: Design, modeling & evaluation of a flat-plate equipment, J. Membr. Sci. 564 (2018) 617–633. https://doi.org/10.1016/j.memsci.2018.07.067.

[64] K. Okiel, A.H.M. El-Aassar, T. Temraz, S. El-Etriby, H.A. Shawky, Vacuum enhanced direct contact membrane distillation for oil field produced water desalination: specific energy consumption and energy efficiency, Desalin. Water Treat. 57 (2016) 11945–11955. https://doi.org/10.1080/19443994.2015.1048305.

[65] E.K. Summers, H.A. Arafat, J.H. Lienhard V, Energy efficiency comparison of single-stage membrane distillation (MD) desalination cycles in different configurations, Desalination. 290 (2012) 54–66. https://doi.org/10.1016/j.desal.2012.01.004.

[66] R.K. Shah, A.L. London, Laminar Flow Forced Convection in Ducts: A Source Book for Compact Heat Exchanger Analytical Data, 1978. https://doi.org/10.1016/B978-0-12-020051-1.50022-X.

[67] R.W. Schofield, A.G. Fane, C.J.D. Fell, Heat and mass transfer in membrane distillation, J. Membr. Sci. 33 (1987) 299–313. https://doi.org/10.1016/S0376-7388(00)80287-2.

[68] L.G. Leal, Advanced transport phenomena: Fluid mechanics and convective transport processes, 2007. https://doi.org/10.1017/CBO9780511800245.

[69] J.H. Ferziger, M. Peric, A. Leonard, Computational Methods for Fluid Dynamics, Phys. Today. (1997). https://doi.org/10.1063/1.881751.

[70] J. Lou, J. Vanneste, S.C. DeCaluwe, T.Y. Cath, N. Tilton, Computational fluid dynamics simulations of polarization phenomena in direct contact membrane distillation, J. Membr. Sci. (2019). https://doi.org/10.1016/j.memsci.2019.05.074.

[71] M. Dudley, 3-D numerical simulations of conjugate heat transport in vacuum membrane distillation systems with applied membrane heating, Colorado School of Mines, 2020.

[72] J. Vanneste, J.A. Bush, K.L. Hickenbottom, C.A. Marks, D. Jassby, C.S. Turchi, T.Y. Cath, Novel thermal efficiency-based model for determination of thermal conductivity of membrane distillation membranes, J. Membr. Sci. (2018). https://doi.org/10.1016/j.memsci.2017.11.028.

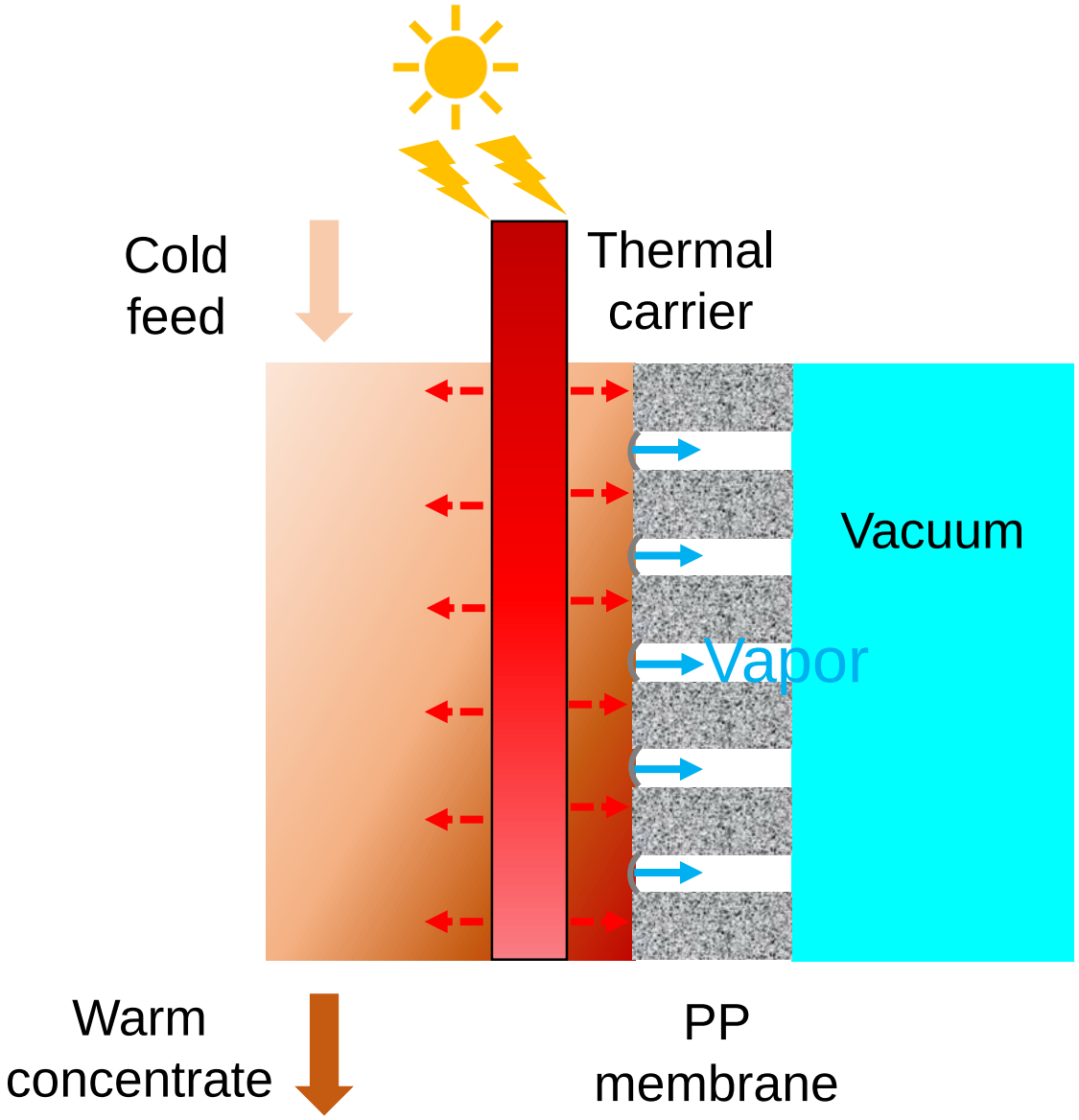
Cold
feed
Thermal
carrier
Vacuum
Vapor
Warm
concentrate
PP
membrane